

1 **WRF-Comfort: Simulating micro-scale variability of outdoor heat** 2 **stress at the city scale with a mesoscale model**

3 Alberto Martilli¹, Negin Nazarian^{2,3}, E. Scott Krayenhoff⁴, Jacob Lachapelle⁴, Jiachen Lu^{2,3}, Esther
4 Rivas¹, Alejandro Rodriguez-Sanchez¹, Beatriz Sanchez¹, Jose Luis Santiago¹

5 ¹Atmospheric Modelling Unit, Environmental Department, CIEMAT, Madrid, 28040, Spain

6 ²School of Built Environment, University of New South Wales, Sydney, Australia

7 ³ARC Centre of Excellence for Climate Extremes, Australia

8 ⁴School of Environmental Sciences, University of Guelph, Guelph, Canada

9 *Correspondence to:* Alberto Martilli (alberto.martilli@ciemat.es)

10 **Abstract.** Urban overheating, and its ongoing exacerbation due to global warming and urban development, leads to increased
11 exposure to urban heat and increased thermal discomfort and heat stress. To quantify thermal stress, specific indices have been
12 proposed that depend on air temperature, mean radiant temperature (MRT), wind speed, and relative humidity. While
13 temperature and humidity vary on scales of hundreds of meters, MRT and wind speed are strongly affected by individual
14 buildings and trees, and vary at the meter scale. Therefore, most numerical thermal comfort studies apply micro-scale models
15 to limited spatial domains (commonly representing urban neighborhoods with building blocks) with resolutions on the order
16 of 1 m and a few hours of simulation. This prevents the analysis of the impact of city-scale adaptation/mitigation strategies on
17 thermal stress and comfort. To solve this problem, we develop a methodology to estimate thermal stress indicators and their
18 subgrid variability in mesoscale models - here applied to the multilayer urban canopy parametrization BEP-BEM within the
19 WRF model. The new scheme (consisting of three main steps) can readily assess intra-neighborhood scale heat stress
20 distributions across whole cities and for time scales of minutes to years. The first key component of the approach is the
21 estimation of MRT in several locations within streets for different street orientations. Second, mean wind speed, and its subgrid
22 variability, are downscaled as a function of the local urban morphology based on relations derived from a set of microscale
23 LES and RANS simulations across a wide range of realistic and idealized urban morphologies. Lastly, we compute the
24 distributions of two thermal stress indices for each grid square combining all the subgrid values of MRT, wind speed, air
25 temperature, and absolute humidity. From these distributions, we quantify the high and low tails of the heat stress distribution
26 in each grid square across the city, representing the thermal diversity experienced in street canyons. In this contribution, we
27 present the core methodology as well as simulation results for Madrid (Spain), which illustrate strong differences between heat
28 stress indices and common heat metrics like air or surface temperature, both across the city and over the diurnal cycle.

30 **1 Introduction**

31 The combination of urban development and climate change has increased heat exposure in cities in recent decades (Tuholske
32 et al., 2021) and a continuation of these trends in the 21st century would be difficult to offset locally from an air temperature
33 perspective (Broadbent et al., 2020; Krayenhoff et al., 2018; Zhao et al., 2021). Adaptation options that target contributions to
34 heat exposure other than the air temperature, such as radiation (e.g., via shade) and wind (e.g. via improved street ventilation),
35 should therefore be considered. Quantification of these contributions relative to air temperature requires the application of
36 comprehensive thermo-physiological heat stress metrics such as the Universal Thermal Climate Index, UTCI (Jendritzky et
37 al., 2012), the Physiological Equivalent Temperature, PET (Höppe, 1999), or the Standard Effective Temperature, SET (Gagge
38 et al., 1986). Moreover, exposure to heat hazards is moderated by infrastructure-based and social/mobility-based adaptations
39 to heat, and by buildings and associated cooling mechanisms. Here, the focus is the development of a tool to quantify the
40 outdoor component of heat exposure in cities, accounting for all relevant meteorological variables.

41 Heat exposure in urban areas is affected by several meteorological variables that vary on different spatial and temporal scales
42 (Nazarian et al., 2022). While temperature and humidity vary on spatial scales on the order of hundreds of meters, shortwave
43 and longwave radiation and wind speed are strongly affected by individual buildings and vary at the scale of a few meters. For
44 this reason, most numerical thermal comfort studies in urban areas apply micro-scale models with resolutions on the order of
45 one m and spatial domains that are limited to an urban block or neighborhood (Nazarian et al., 2017; Zhang et al., 2022; Geletič
46 et al., 2018). While these studies include substantial detail at the micro-scale, they are very expensive computationally and
47 therefore can be applied only to a few neighborhoods and they neglect the interactions with larger scale meteorological
48 phenomena (e.g., land/sea breezes, mountain/valley winds, urban breezes) that often play a relevant role in outdoor thermal
49 comfort and its variation across cities. On the other hand, contemporary meso-scale numerical models can be applied to the
50 whole urban area and surrounding regions, and therefore capture these larger-scale phenomena, but have spatial resolutions of
51 several hundred meters at best. These models use a grid mesh that does not resolve buildings and is therefore too coarse to
52 capture the fine-scale variation of radiation and wind flow of relevance to outdoor heat exposure and ultimately thermal
53 comfort.

54 The objective of this work is to fill the aforementioned gap by developing a model that includes the most crucial capabilities
55 of micro-scale assessments of thermal exposure within meso-scale models. This new model will quantify the spatial variability
56 (i.e., statistical representation of the microscale distribution) for longwave and shortwave radiation as well as wind speed
57 within each meso-scale grid square. Subsequently, it will capture the range of thermal exposure, as quantified by the UTCI
58 and SET thermal stress metrics, within each urban grid square across a city at each time of day. The focus here is on the *range*
59 of thermal exposure, such that we identify the cool and hot spots within the grid cell without having to resolve the entire spatial
60 distribution. We argue that this represents the most crucial information for heat management and urban design interventions,
61 as it identifies whether people can move and search for optimal thermal conditions. For example, if hot spots are experiencing
62 extreme heat stress but the cool spots are at slight heat stress, pedestrians have the opportunity, and autonomy, to seek shade

63 and thermal respite (i.e., temporal and spatial autonomy as described in Nazarian et al. (2019)). Conversely, if the conditions
64 in the cool spot are already in extreme heat stress, this can be used to inform urban design interventions or heat advisories to
65 vulnerable populations to avoid being outside at that place and time. Overall, representing the range of heat exposure at the
66 neighborhood scale while covering regional-scale phenomena is key to human-centric assessments of urban overheating
67 (Nazarian et al., 2022).

68 The new model is embedded in the multi-layer urban canopy parameterization BEP-BEM (Martilli et al., 2002; Salamanca et
69 al., 2010) which simulates the local-scale meteorological effects of the grid-average urban morphology within the Weather
70 Research and Forecasting (WRF) mesoscale model (Skamarock et al., 2019 version 4.3 has been used in this study). Here,
71 BEP-BEM is extended to quantify the spatial variation of the mean radiant temperature and wind speed within the grid square
72 at the pedestrian level. To our knowledge, three schemes in the published literature have attempted to capture thermal exposure
73 in an urban canopy model. Pigliautile (2020) implemented a scheme to estimate human thermal exposure in the Princeton
74 Single-Layer Urban Canopy Model. However, the scheme has not been run within a mesoscale model. Jin et al. (2022) calculate
75 urban mean radiant temperature (MRT) in a mesoscale model, while Lemonsu (2015) and Leroyer et al. (2018) assess UTCI
76 in mesoscale modeling applications within Paris and Toronto, respectively. Moreover, Giannaros et al (2018, 2023), made an
77 offline coupling of WRF-BEP_BEM with RayMan (Matzarakis et al. 2007). However, none of these approaches account for
78 the within-grid spatial variation of wind speed, and their assessment of sub-grid spatial variation of radiation exposure (i.e.,
79 mean radiant temperature) is limited. Here, we further extend the BEP-BEM model embedded in the WRF meso-scale model
80 to overcome these limitations and better assess spatial variation of thermal exposure within each urban grid square.

81 In section 2, the methodology is described in detail, with a focus on model development and implementation in WRF. In
82 Section 3, we present an example of the type of outputs that can be produced. Conclusions are in section 4.

83 **2 Methodology**

84 The most complete thermal stress indices invariably depend on four meteorological variables: air temperature, mean radiant
85 temperature (MRT), relative humidity, and wind speed. Among these, MRT and wind speed have the largest spatial variability
86 in the urban canopy, and this variability is often captured with 3D micro-scale models of urban airflow and radiative heat
87 transfer. At the meso-scale, however, it is not feasible to incorporate such models, motivating the simplified urban canopy
88 parameterizations developed here. Below we detail how the BEP-BEM urban canopy model is modified to a) introduce a
89 simplified model for MRT variation within a meso-scale grid cell (Sec. 2.1) and b) parameterize airflow variability (Sec. 2.2)
90 in the urban canopy within a grid cell, and make a simple estimate of air temperature variability. These meteorological
91 parameters are then used to estimate the sub-grid scale variation of thermal stress indices (Sec. 2.3), namely SET and UTCI,
92 as two of the most commonly used indices for outdoor environments (Potchter et al 2018). Lastly, we discuss how multi-scale

93 temporal and spatial variabilities in thermal exposure can be effectively communicated using the outcomes of the updated
94 WRF-BEP-BEM model.

95 **2.1 A simplified model for MRT variability in the urban canopy**

96 The mean radiant temperature is a measure of the total radiation flux absorbed by the human body, including both shortwave
97 (from the sun, either directly or after reflection on the walls or road) and longwave (emitted from solid bodies like walls or
98 road, or from the sky) radiation. Whether pedestrians are shaded or in the sunshine, as well as their distance from warm surfaces
99 emitting radiation, is therefore very important. BEP-BEM applies a simple urban morphology: two street canyons of different
100 orientations, each with the same street width and building height distribution on each side of the canyon (Martilli et al. 2002).
101 To capture the within-grid spatial extremes of mean radiant temperature, we assess pedestrian locations at the center of the
102 street for two canyon orientations considered in BEP-BEM and at positions located at a distance of 1.5 m from the building
103 wall on each side of the street, representing the sidewalks. Thus, there are 6 positions (three for each street direction) in each
104 urban grid square where we compute the mean radiant temperature (shown for the example of North-South and East-West
105 streets in Fig. 1). For shortwave and longwave radiation exchange, the standard BEP view factor and shading routines (Martilli
106 et al. 2002) are used to estimate the amount of shortwave (direct and diffuse) and longwave radiation reaching a vertical
107 segment 1.80 m tall and located in each of the six positions previously mentioned (Fig. 1, Appendix A). Reflection of shortwave
108 radiation and emission and reflection of longwave radiation from both building walls and the street surface are accounted for
109 via these view factors. The pedestrian is “transparent” from the perspective of the urban facets, meaning that its presence does
110 not alter the shortwave and longwave radiation reaching the building walls and road. The mean radiant temperature is computed
111 by weighting the radiation reaching each side of the vertical segment by 0.44, and the radiation reaching the downward- and
112 upward-facing (at 1.80 m height) surfaces of the pedestrian by 0.06 each. This approach follows the six-directional weighting
113 method (Thorsson et al. 2007) and aggregates the four lateral weightings of 0.22 into two lateral weightings of 0.44 since BEP-
114 BEM is a two-dimensional model (e. g. the streets are considered infinitely long). Namely,

$$115 \quad T_{MRT} = \sqrt[4]{\frac{\sum_{i=1,4} W_i (a_K K_i + a_L L_i)}{a_L \sigma}} \quad (1)$$

116 where, for a N-S oriented street, $i=1,2$ are for the vertical sides of the pedestrian looking East, and West respectively, and $i=3,4$
117 are for the top and bottom. Therefore, $W_{1,2}=0.44$, while $W_{3,4}=0.06$, while the absorptivity of the pedestrian in the shortwave
118 and longwave, a_K (the absorption coefficient for shortwave radiation of the human body) and a_L (the absorption coefficient for
119 long-wave radiation, or emissivity, of the human body), respectively, are $a_K=0.7$, and $a_L=0.97$, $K_{1,2}$ and $L_{1,2}$ are the short and
120 longwave radiation reaching the vertical segment, and $K_{3,4}$ and $L_{3,4}$ are short and longwave radiation reaching the top and
121 bottom respectively, and σ is the Stefan-Boltzmann constant (see Appendix A for details about how the radiation components
122 are computed).

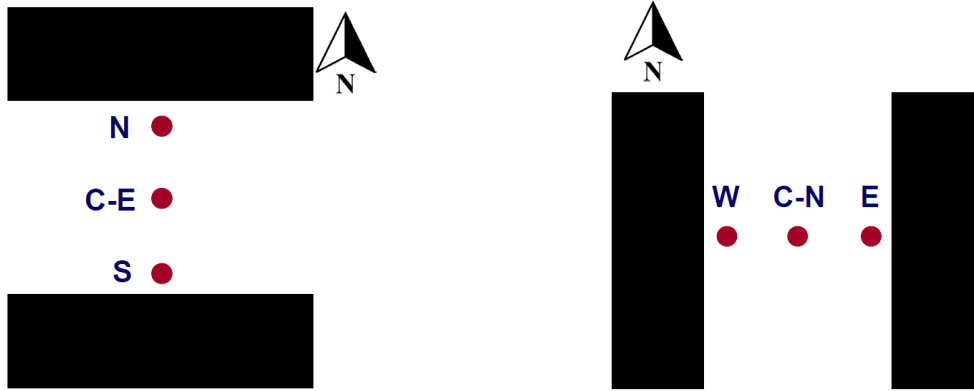


Figure 1: Two street directions (left: E-W canyon, right: N-S canyon) and pedestrian locations considered for Mean Radiant Temperature calculations.

123 The diurnal progression of the mean radiant temperature computed by this new model in BEP-BEM is subsequently compared
 124 with that obtained from TUF-Pedestrian, a more detailed three-dimensional model that has been evaluated against
 125 measurements (Lachapelle et al. 2022; Jiang et al. 2023). TUF-Pedestrian is configured with identical input parameters and
 126 meteorological forcing, and with long canyons that approximate the two-dimensional BEP-BEM canyon geometry. The new
 127 model clearly captures the relevant details of the diurnal progression of MRT at all six locations (Fig. 2), with a mean absolute
 128 difference of 3.4 K, and a root mean square difference of 4.3 K across all locations. A comparison of the shortwave radiation
 129 loading on the pedestrian between the two models reveals very good agreement (Appendix B Fig. B1, B2), considering the
 130 highly simplified urban morphology used by BEP-BEM, with biggest errors limited to short periods of time; thus, most of the
 131 model disagreement arises from differences between longwave loading on the pedestrian as a result of different methods for
 132 computation of surface temperature between the models. Overall, the new model of mean radiation temperature in BEP-BEM
 133 provides satisfactory results.

134

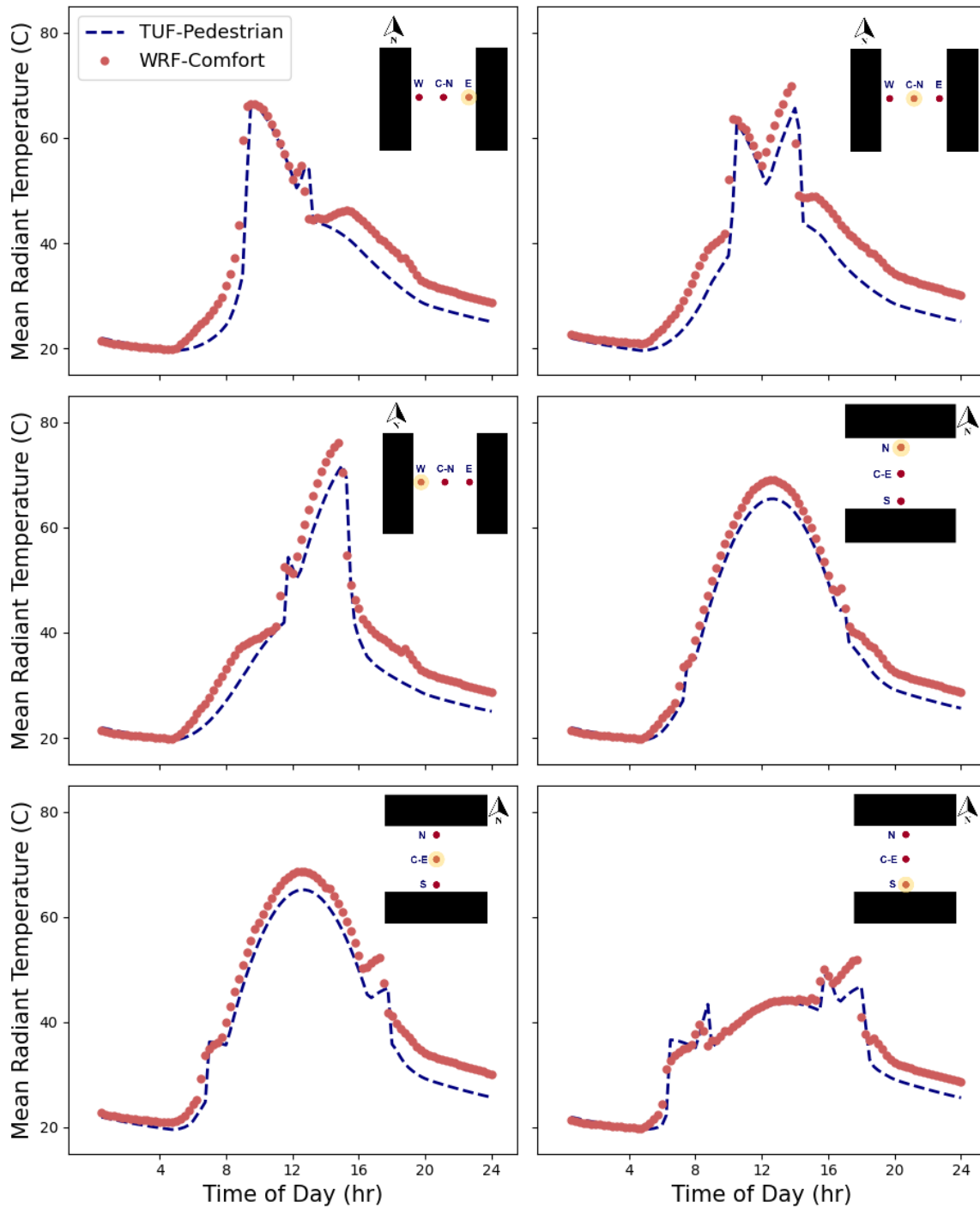


Figure 2: Comparison of diurnal variation of Mean Radiant Temperature (MRT) between the new model in BEP-BEM and TUF-Pedestrian for each of the six locations in Fig. 1. TUF pedestrian acts here as a reference.

135

136

137

138 **2.2 Parameterize airflow variability in the urban canopy**

139 Mesoscale models solve conservation equations for the three components of momentum. From these, it is possible to derive
 140 the spatially averaged wind velocity in each grid cell, at the grid resolution of the mesoscale model, commonly of the order of
 141 300m-1km. The spatially averaged wind velocity in the urban canopy $\langle V \rangle$, close to the pedestrian height ($\sim 2.5\text{m}$), is the square
 142 root of the sum of the spatial average of the two horizontal components u , and v , (neglecting the vertical component, which is
 143 usually at least one or two orders of magnitude smaller than the horizontal),

$$144 \langle V \rangle = \frac{1}{V_{air}} \sqrt{\left(\int_{V_{air}} u dV \right)^2 + \left(\int_{V_{air}} v dV \right)^2} \quad (2)$$

145 where here V_{air} is the volume of the grid cell occupied by air (e. g. without the buildings)

146 However, the wind velocity calculated in mesoscale models is different from the average wind speed that would be experienced
 147 by a person in the grid cell. This is better represented by the spatial average of the wind speed $\langle U \rangle$ (e. g. the modulus of the
 148 vector), written as

$$149 \langle U \rangle = \frac{1}{V_{air}} \int_{V_{air}} \sqrt{u^2 + v^2} dV \quad (3)$$

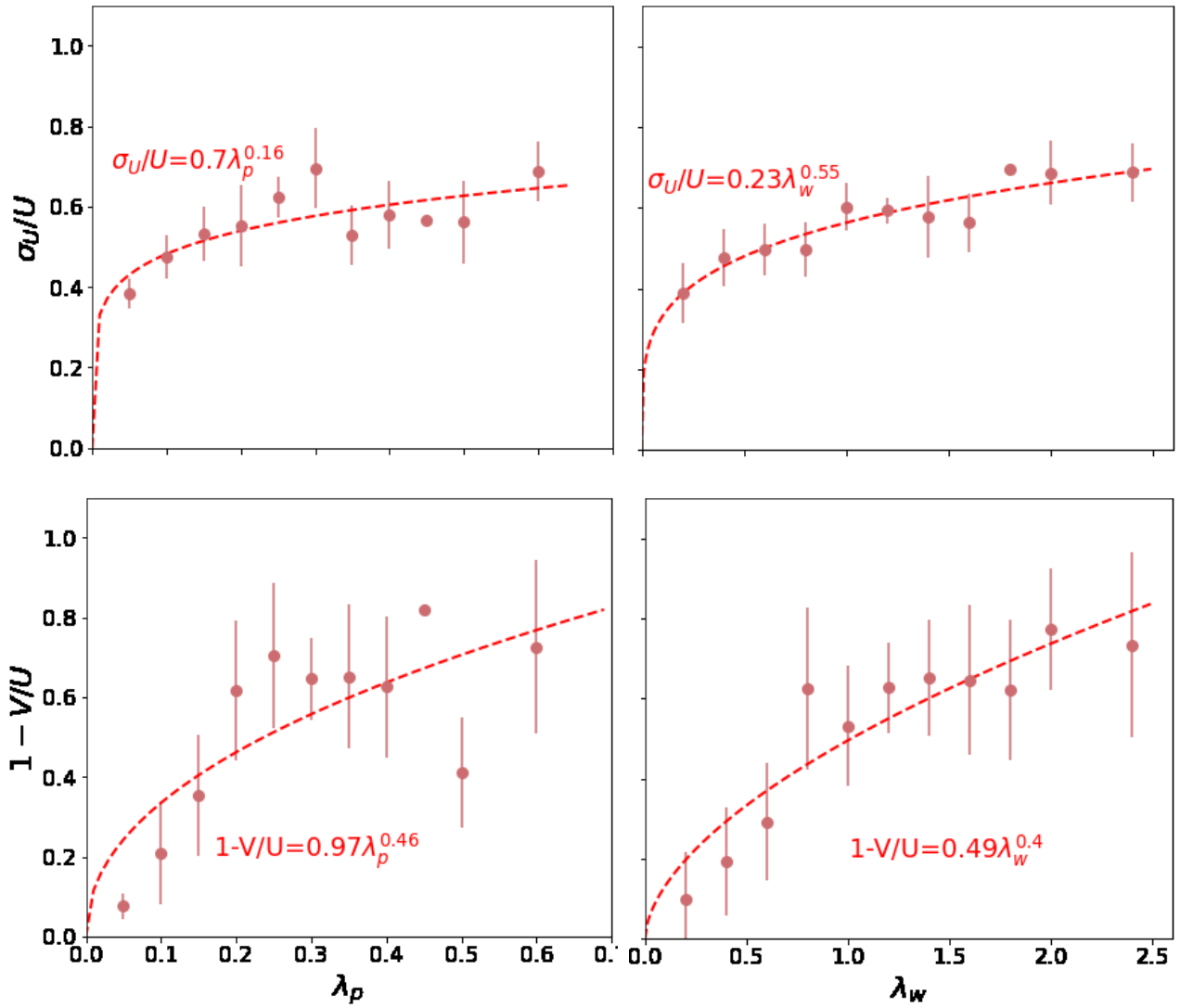
150 To assess the impact of airflow on human thermal comfort, the wind speed should be estimated from the wind velocity
 151 computed in the mesoscale models. Additionally, it is critical to parameterize and estimate the spatial variability of mean wind
 152 speed in the urban canopy. Accounting for these factors, the range of wind speed variability at the pedestrian level is estimated,
 153 which is critical for the quantification of spatial variability of outdoor thermal stress and comfort.

154 Here, we describe the parameterization of a) wind speed-to-velocity ratio and b) wind speed distribution, based on urban
 155 density parameters. Data are considered from over 173 microscales CFD simulations of urban airflow over realistic and
 156 idealized urban configurations, spanning a wide range of building plan area (λ_p), frontal area (λ_f), and wall area (λ_w) densities
 157 representative of realistic urban neighbourhoods in different types of cities. CFD simulations are conducted using 162 large-
 158 eddy simulations (LES) and 11 Reynolds-averaged Navier–Stokes (RANS) schemes detailed in Appendix C.

159 Mean wind velocity $\langle V \rangle$, speed $\langle U \rangle$ and its spatial standard deviation (σ_U) are computed at a horizontal cross-section at
 160 pedestrian height for each CFD simulation and used for deriving parameterizations (Fig. 3). An additional data point is added
 161 at $\lambda_p=\lambda_w=0$, ensuring that wind speed is equal to wind velocity, and its standard deviation is set to zero, for the non-urban case.
 162 It is important to remark here, that we are dealing with the standard deviation of the spatial distribution of the mean wind
 163 speed. With the term *mean* we indicate the result of an ensemble (over many realizations) or time average (over time scales
 164 larger than the turbulence time scale, but smaller than the time scale of the mesoscale motions), but not a spatial average. The
 165 urban canopy, in fact is spatially heterogeneous, and, for this reason, the time and ensemble averages are different than the
 166 spatial average. Only when $\lambda_p=\lambda_w=0$ (e. g. there are no buildings), and the horizontal homogeneity is recovered, must the

167 variability be zero. This σ_U , therefore should not be confounded with the turbulent σ , that indicates the variability in
 168 instantaneous wind speed induced by turbulent motions, which indeed is not zero even when there are no buildings.

169



170 **Figure 3:** Relationship between $1 - \langle V \rangle / \langle U \rangle$ (bottom row), and $\sigma_U / \langle U \rangle$ (top row), and two morphological parameters, λ_p (left column), and
 171 λ_w (right column) based on the CFD simulations. Dots represent the average of the value among all the simulations that share the same
 172 morphological parameter, and the vertical bar indicates the standard deviation. The dashed line and the formula indicate the best fit.

173

174 Parameterizations are derived (shown in Fig. 3) for two density parameters ($\lambda_p=Ap/Atot$, and $\lambda_w=Aw/Atot$, where A_p is the
175 area of the horizontal surface occupied by buildings, or the roof area, A_w is the area of vertical (wall) surfaces, and A_{tot} is the
176 total horizontal area). We find that λ_w better predicts mean wind speed and its spatial variability at the pedestrian height,
177 because it represents both horizontal and vertical heterogeneities in the urban canopy. Note that λ_F has not been included in
178 the study, given the difficulty to estimate it for real urban areas, and to translate it to the simplified 2D urban morphology used
179 by BEP-BEM. In any case, λ_F is closely related to λ_w . Therefore, the following parameterizations are implemented at the
180 pedestrian height as a function of the wall area density λ_w

181

$$182 \quad \langle U \rangle = \frac{\langle V \rangle}{1 - 0.49\lambda_w^{0.4}} \quad (4)$$

$$183 \quad \sigma_U = \langle U \rangle (0.25\lambda_w^{0.55}) \quad (5)$$

184 We, therefore, assign three values of wind speed in each grid cell,

$$185 \quad \langle speed \rangle_1 = \max(0.01, \langle U \rangle (1 - 0.25\lambda_w^{0.55}))$$

$$186 \quad \langle speed \rangle_2 = \langle U \rangle \quad (6)$$

$$187 \quad \langle speed \rangle_3 = \langle U \rangle (1 + 0.25\lambda_w^{0.55})$$

188 Note that here we consider the three values equally likely, in order to realistically span the range of possible values that the
189 wind speed can take in each grid cell. Since UTCI has been designed for 10m wind speeds, a simple log law is used to
190 rescale wind speed at 10m, before passing it to the UTCI routine.

191 **2.3 Calculation of the thermal comfort index**

192 To represent the subgrid spatial variability of air temperature, detailed CFD simulations are not available, so we simply use a
193 variability of 1 degree Celsius, which we consider to be a conservative estimate of the spatial variability of air temperature
194 over a spatial scale of the order of one km². This value is consistent with the range obtained in the few non-natural simulations
195 available, like Santiago et al. (2014), and Nazarian et al. (2018) over idealized arrays, as well as that obtained by Rivas-
196 Ramos over a realistic neighbourhood of Madrid (2024, personal communication). A better determination of the variability is
197 left to future studies. Therefore, for each grid cell, we have three values for air temperature:

$$198 \quad Temp_1 = Temp_{WRF} - 1$$

$$199 \quad Temp_2 = Temp_{WRF} \quad (7)$$

$$200 \quad Temp_3 = Temp_{WRF} + 1$$

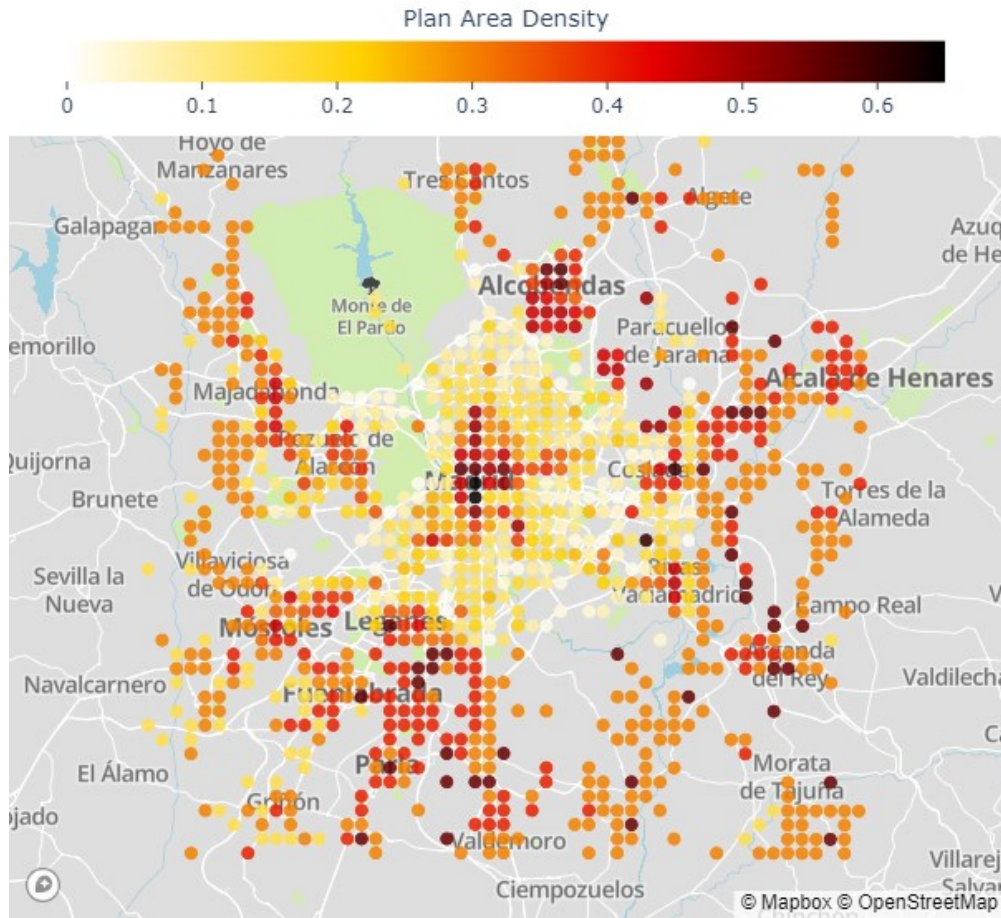
201 where $Temp_{WRF}$ is the air temperature provided by WRF.

202 We therefore have, for each urban grid cell, *three* values of wind speed, *three* values of temperature, and *six* values of mean
203 radiant temperature. No variability of the absolute humidity is considered, but the relative humidity is computed using the
204 three values of air temperature.

205 Based on the variation of these climate variables, assumed uncorrelated, 54 possible combinations of the air temperature, mean
206 radiant temperature, and wind speed values can be formed. For each one of these combinations, we calculate the corresponding
207 SET or UTCI value. Based on the resulting distribution, we estimate the value of the 10th, 50th, and 90th percentile SET or
208 UTCI for each grid square (at each output time). Increasing the number of points where the mean radiant temperature is
209 computed, or adding more values for the wind speed, does not change significantly the values of the percentiles (not shown).

210 **3. Characterization of thermal comfort in regional-scale models: Madrid case**

211 To illustrate the capabilities of the new scheme, a typical heat wave day in the city of Madrid (Spain) is simulated with WRF.
212 Madrid is located on a plateau at 500-700m above sea level, in the middle of the Iberian Peninsula. It experiences hot summers,
213 with frequent heat waves that increasingly cause severe heat stress in the population, and it is therefore considered a relevant
214 case study. Four nested domains have been used, with resolutions of 27, 9, 3, and 1km respectively. The city morphology (Fig.
215 4) is derived from high-resolution LIDAR data that covers most of the metropolitan area of Madrid (Martilli et al., 2022),
216 while the morphology of the surrounding towns is determined based on Local Climate Zone maps (Brousse et al., 2016). It is
217 also important to mention that the city is located on a hilly terrain, with higher elevations in the N-W part of the urban area
218 (around 700m a.s.l.) dropping to 500m a.s.l. or less in the S-E. Moreover, there are two topographical depressions on the two
219 sides of the city centre, caused by the rivers Jarama and Manzanares (for a detailed description of the topography see also
220 Martilli et al. 2022, where the same set-up was used). Other model configurations are the NOAH vegetation model for the
221 non-urban grid points and the Bougeault and Lacarrere (1989) PBL scheme for turbulence parameterization. WRF coupled
222 with BEP-BEM has previously been successfully used to simulate a heat wave period in Madrid (Salamanca et al., 2012). The
223 period used in this paper is three days (14-16 July 2015). In particular, the analysis will focus on the 15th, when the maximum
224 simulated temperature was above 40 Celsius. More information about the validation and a sensitivity study to select the optimal
225 set-up can be found in Rodriguez-Sanchez (2020).



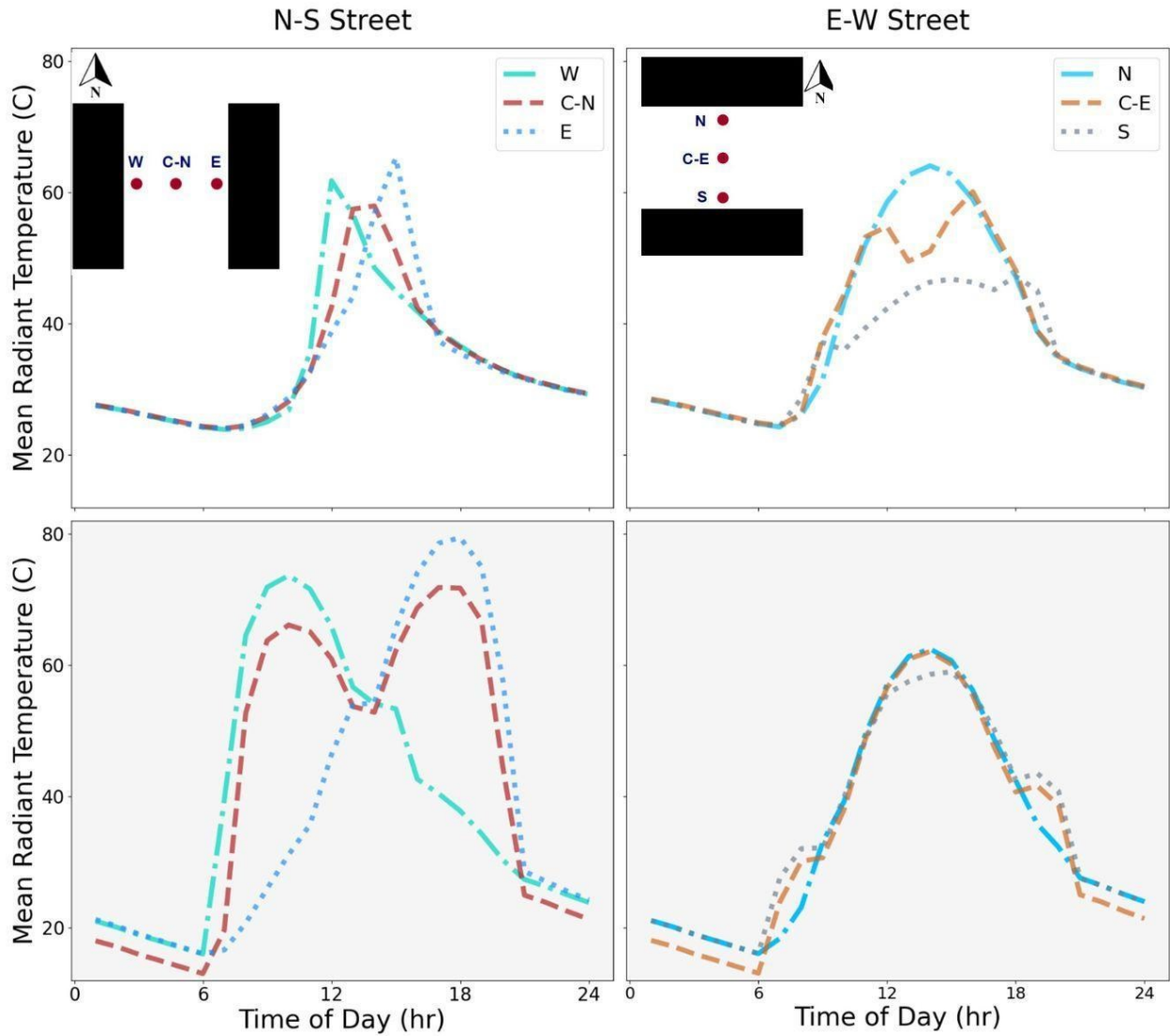
226

227 **Figure 4.** Map of the plan area building density over the Madrid region. The underlying map was created with Mapbox OpenStreetMap.
 228 The map is oriented so that left is west, and up is north, and the size is 50x50km.

229 **3.1 Sub-grid scale variability of MRT and thermal comfort.**

230 In order to understand how urban morphology affects the simulated heat stress, we focus on two grid points with very different
 231 urban morphology. One is located in the dense core of the city, with a building plan area density of $\lambda_p = 0.69$, and a height-to-
 232 width ratio (H/W) value of 1.6. The second is located in the southern part of the urban area, in a residential neighbourhood
 233 with a much lower building density ($\lambda_p = 0.2$) and a H/W=0.1.

234 In Figure 5, the diurnal evolution of the mean radiant temperature in the six points (three per street direction) is presented for
 235 the high urban density point and the low urban density point. During the daytime, the impact of the shadowing is clear, with
 236 reduced mean radiant temperature in the high-density point compared to the more exposed low-density. On the other hand,
 237 during night-time, the reduced sky-view factor in the high-density point slows down the cooling compared to the more open
 238 low-density location.

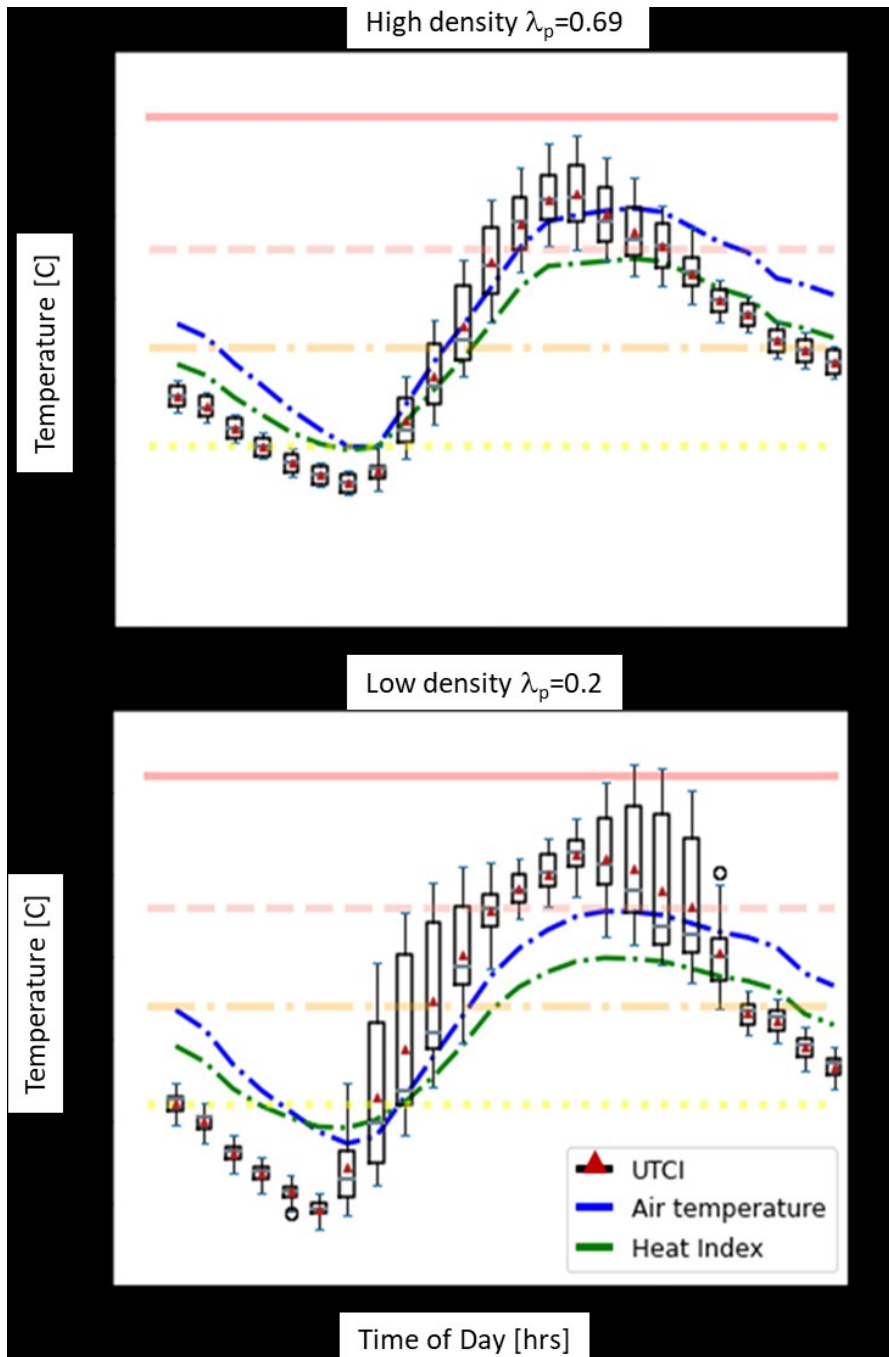


239

240 **Figure 5.** Diurnal evolution of MRT for 6 points in the urban canopy. The top row (white background) corresponds to a grid point with the
 241 highest building density in the centre of Madrid ($\lambda_p = 0.69$) while the bottom row (with grey background) shows MRT in a low-density
 242 neighbourhood ($\lambda_p = 0.19$). The left column is for an N-S street, while the right column shows an E-W street.

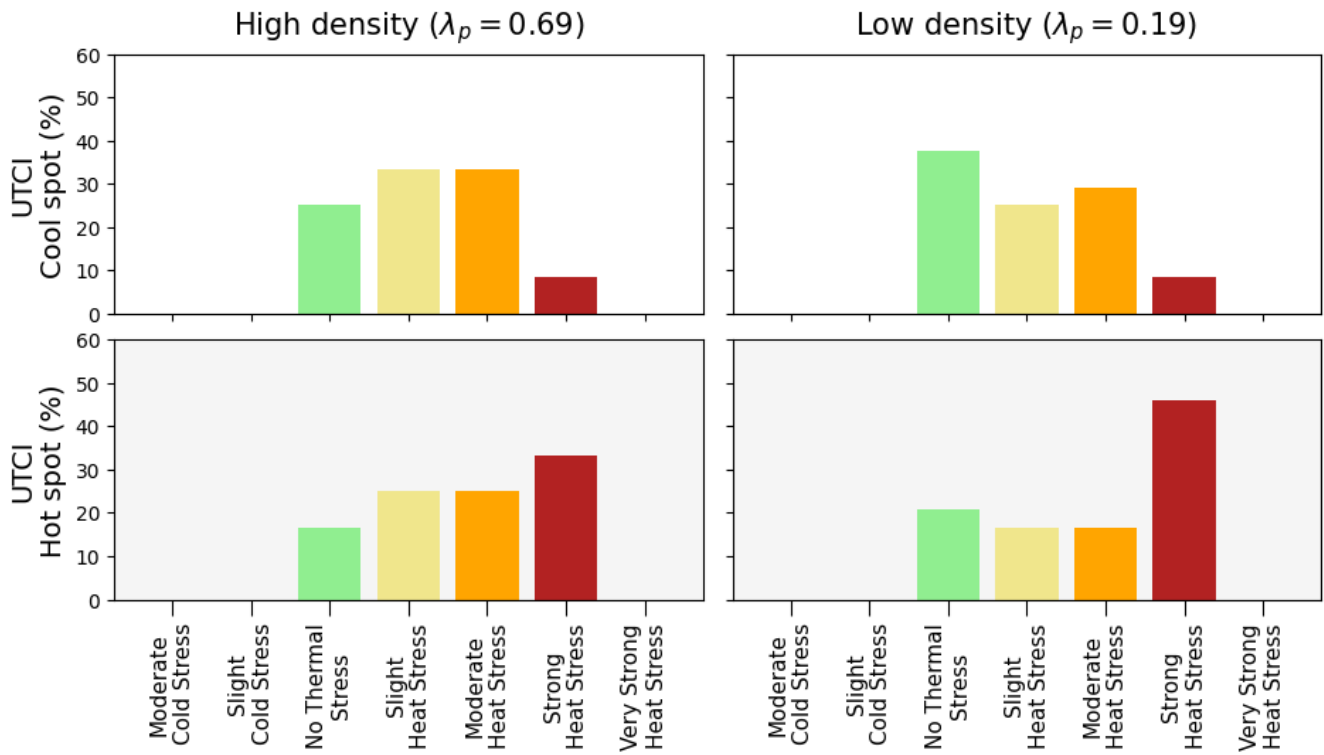
243 This behaviour helps to explain the heat stress index (Figure 6), which is introduced here as an example of an index that can
 244 be computed with standard outputs from meteorological models, i.e., without information related to the radiation environment

245 (e.g., MRT) and urban morphology. The air temperature indicates hotter values both during the day and the night in the high
246 urban density point compared to the low-density location. The Heat Index, which considers air temperature and humidity only,
247 and does not include mean radiant temperature or wind, shows the same tendency. On the other hand, the UTCI behaviour
248 communicates a different and more complete result. In the low-density neighbourhood, more exposed to the sun, the UTCI
249 shows a stronger sub-grid spatial variability, in particular during the morning and afternoon, with the potential for stronger
250 heat stress than in the high-density neighbourhood. During night-time, the spatial variability is reduced, due to reduced MRT
251 variation as the shadowing effect disappears, and higher UTCI values are found at the high urban density location. This
252 difference in behaviour between the two locations can be seen also in Fig. 7, where the fractions of the 10th percentile of UTCI
253 values (i.e. representative of one of the coolest spots in the grid cell) and the 90th percentile (i.e., one of the hottest) in the
254 different heat stress regimes are shown for the two points. Here we can see that in the low-density urban point, the cool location
255 is in a comfortable UTCI range most of the time, while the hot (90th percentile UTCI) sub grid location is under stress most
256 of the time. On the other hand, less variability is present in the high-density neighbourhood, with fewer extreme values, and
257 most of the time in the strong or moderate heat stress regime for both the cool and hot locations within the grid square. This
258 kind of detail is not available from the Heat Index distribution which does not account for the mean radiant temperature, wind,
259 or their variabilities (Fig. 8).



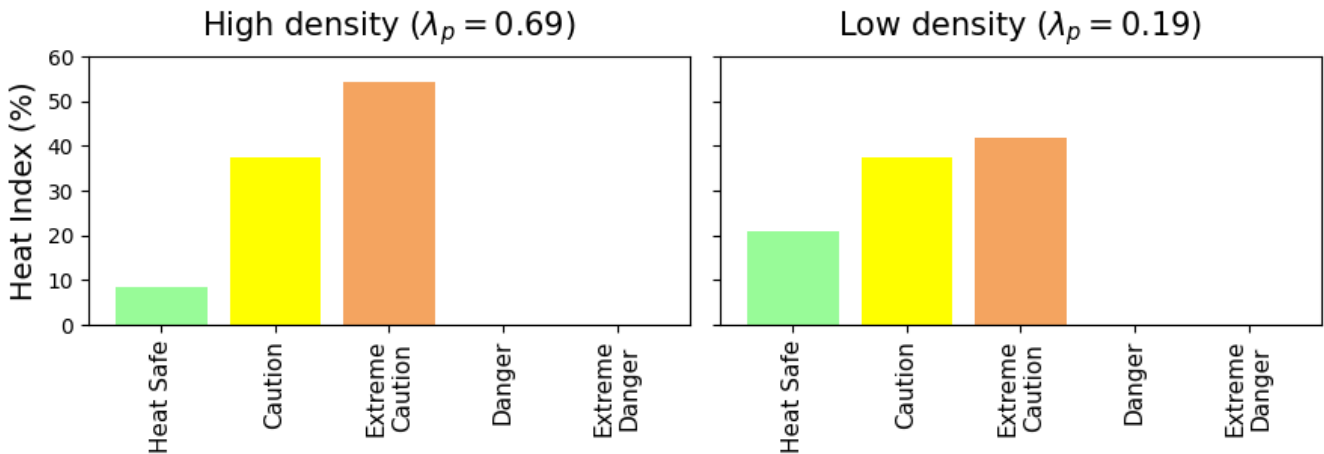
260
261
262
263
264
265

Figure 6. Diurnal evolution of UTCI compared with 2-m air temperature and Heat Index calculated from air temperature and relative humidity at each grid point). The UTCI boxplot at each hour represents the subgrid-scale distribution calculated based on 6 MRT, 3 wind speeds, and 3 air temperature values (54 combinations in total). The horizontal lines represent the thermal comfort zones for UTCI (i.e. above +46C: extreme heat stress; +38 to +46: very strong heat stress; +32 to +38: strong heat stress; +26 to +32: moderate heat stress; and +9 to +26: no thermal stress).



266
267
268
269
270

Figure 7. From top to bottom, the frequency of UTCI class over a 24-hour period, for a subgrid location that is cooler (i.e. 10th percentile of UTCI in the urban canopy, top), and for a subgrid location that is hotter (i.e. 90th percentile of UTCI in the urban canopy, bottom), for the high-density (left) and low-density (right) points.



271
272
273

Figure 8. same as Figure 7, but for the Heat Index

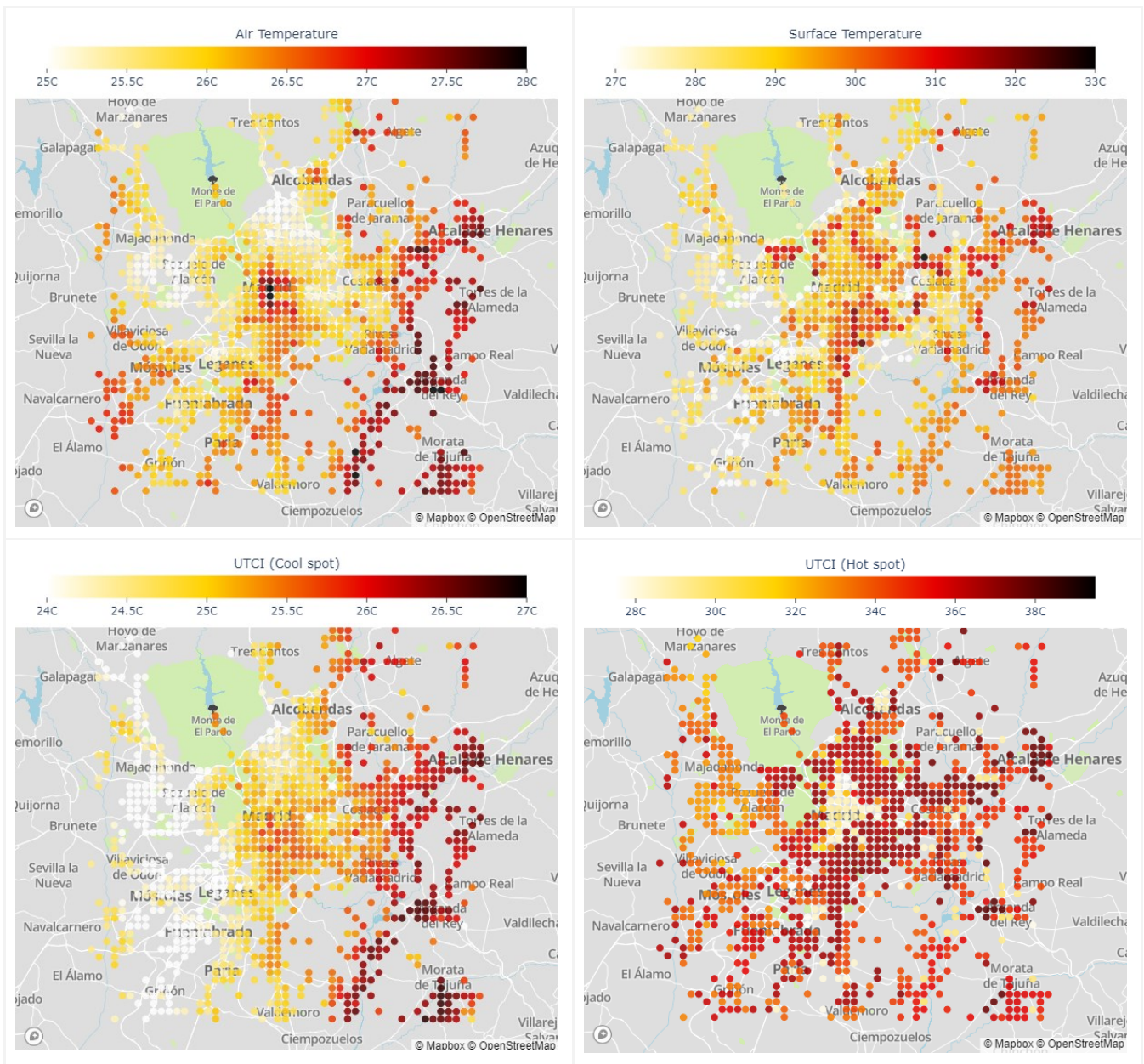
274 **3.2 City-scale maps of outdoor thermal comfort and heat stress indicators.**

275 The previous analysis helps to understand the spatial distribution of the different variables presented in Fig. 9 at 10 and 16
276 UTC (note that Madrid is at Longitude 3W, so UTC is essentially equal to solar time). In the dense city centre, the distribution
277 of 2m air temperature at 0900 UTC shows a hot region, with cooler areas in the less dense regions around it. This effect is due
278 to the fact that in the dense region, the reduced sky-view factor of the streets (high H/W), as well as the larger thermal storage
279 capacity in the buildings, reduce the nocturnal cooling, and increase the vertical mixing in that part of the city compared to the
280 surroundings. Such a difference is still visible in the morning. The higher temperatures in the S-E part of the urban area, and
281 cool temperatures in the N-W are the result of the topographical differences. The spatial distribution of air temperature is
282 qualitatively similar to the spatial distribution of the 10-percentile of UTCI (e. g. the cool spot in the grid cell), even if the
283 differences between the centre and the surrounding urban areas are not as intense as for 2m air temperature. On the other hand,
284 the 90-percentile map (hot spot), shows a completely different pattern; on the city centre, at that time of the day, the whole
285 street is still in the shadow, while in the surrounding, less dense urban areas, there are points completely exposed to the sun.
286 As a comparison, the map of surface temperature (a variable often used to represent the spatial distribution of heat in cities) as
287 seen from a satellite, i.e. based only on a weighted average of roof, street, and vegetation temperatures (see full equations in
288 Martilli et al. 2021), does not show a clear pattern, and it is uncorrelated with the other maps. This is a clear indication that
289 this variable should not be used for the assessment of the heat hazard or heat stress in urban areas.

290 At 1600 UTC the air temperature shows again higher values in the city centre, lower in the urban surroundings, and a gradient
291 from hotter S-E at lower elevations to cooler N-W at higher elevations (Fig. 10). Such a tendency is present also for the 10th
292 percentile (cool spot), but with less variability. The 90th percentile map (hot spot) indicates that the area with elevated heat
293 stress extends well beyond the city centre, including lower-density regions that, even if they have lower air temperatures, are
294 fully exposed to the sun. Finally, as it was the case for 0900 UTC, the surface temperatures have a map uncorrelated with
295 neither the air temperatures nor the UTCI maps.

296

297



298

299

300

301

302

303

304

Figure 9. Spatial maps at 0900 UTC for 2-m air temperature (top left), surface temperature (top right), UTCI cool spot e. g. the 10 percentile of UTCI captured in the urban canopy model (bottom left), and UTCI hot spot e. g. 90 percentile of UTCI in the urban canopy (bottom right). Surface temperature is equivalent to that seen by a nadir-view satellite sensor (i.e., an area-weighted average of canopy ground temperature, roof temperature, and vegetation temperature in non-urban fractions is considered). The underlying maps were created with Mapbox OpenStreetMap

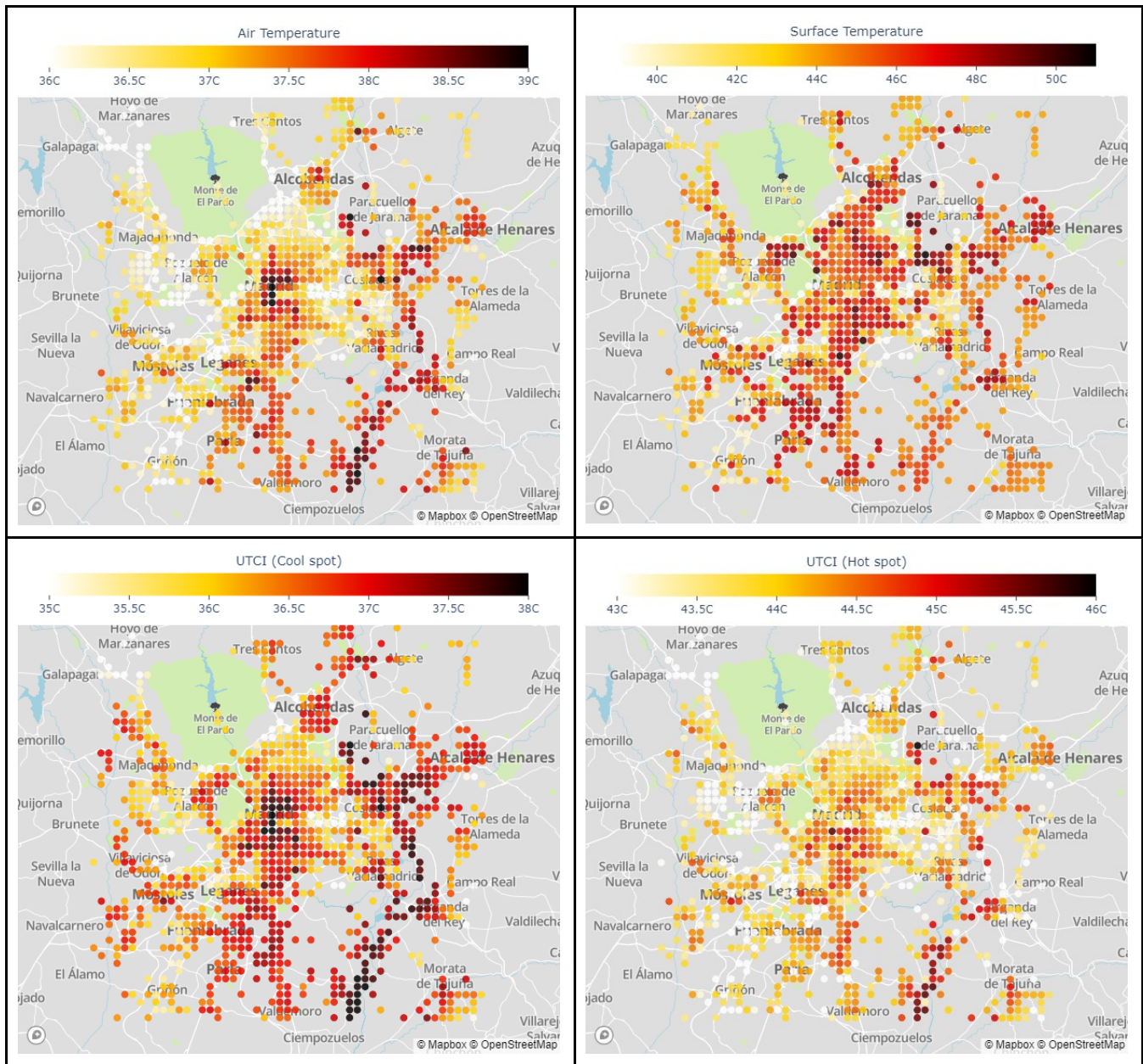


Figure 10. Same as Figure 9, but at 1600 UTC.

4. Limitations

310 The main limitation of the approach we propose here to account for the sub-grid variability of mean radiant temperature is the
311 idealization of the urban morphology adopted by the urban canopy parameterization BEP-BEM. This consists of representing
312 the urban morphology as a series of infinite urban canyons, all with the same width, separated by buildings of constant width,
313 and variable building height. Two street orientations are considered for each grid cell: North-South, and East-West. The
314 dimensions of the buildings and street canyons are determined such that the building plan area density, the density of urban
315 vertical surfaces per horizontal area, and the mean building height are equal to those of the real morphology of the grid cell.
316 As a result, the total surface areas of walls, roads and roofs in the idealized morphology used by BEP-BEM closely approximate
317 the corresponding surface areas in the real neighbourhood, and – to a certain extent – the street and buildings of the idealized
318 morphology can be considered representatives of an average street and set of buildings present in the grid cell. The advantage
319 of this approach, common among the most widely-used urban canopy parameterizations (Masson, 2000, Kusaka et al. 2001),
320 is that it allows accurate estimation of shadowing and radiation trapping effects in the urban canopy with low computational
321 cost, without considering the real urban morphology. Keeping the computational cost low was an essential requirement
322 considering the computational resources available when these urban canopy parametrizations were developed (about 20 years
323 ago). With today’s computational resources, there may be potential to account for more complexity in the urban morphology.
324 However, this would require deep changes in the structure of the urban canopy parametrization BEP-BEM that are beyond the
325 scope of the present article. For this reason we decided to keep the idealized morphology of BEP-BEM and estimate the mean
326 radiant temperature in six locations representative of the middle of the street and the sidewalks. So, the mean radiant
327 temperatures computed are representatives of those six points of an “average” street in the grid cell. Indeed, in a grid cell of a
328 mesoscale model (that typically has a size of the order of one km²) there is a variety of street and building dimensions and
329 orientations, so the present approach cannot capture the full spatial variability of mean radiant temperature, a variability that
330 increases with the heterogeneity of the real urban morphology. Nevertheless, it represents a step forward, since it accounts for
331 the range (and to some extent, the variability) of mean radiant temperature within the “average” idealized street canyon, that
332 can be reasonably considered the most likely street typology within the grid cell, something that previous approaches does not.
333 Overall, the current approach is likely to accurately quantify the mean radiant temperature of at least one “average” shaded
334 pedestrian and one “average” sunlit pedestrian (during periods with direct shortwave irradiance), and thus capture the largest
335 source of spatial variation of both MRT and UTCI (Middel and Krayenhoff, 2019). Another limitation of the approach
336 presented here is the lack of street trees. Currently work is in progress to introduce trees in the version of BEP-BEM
337 implemented in WRF via implementation of the BEP-Tree model (Krayenhoff et al. 2020), and in this way account for their
338 impacts on mean radiant temperature as well as on air temperature, humidity, and wind.

339 The approach used to estimate the mean wind speed and its sub-grid variability is grounded on a large number of CFD
340 simulations over a variety of urban morphologies. Indeed, as shown in Fig. 3, the sub-grid variability of wind speed can be
341 quite large, and certainly strongly influenced by the relative arrangements of buildings and streets. So, the approach presented
342 here will likely underestimate the sub-grid variability of wind speed – and this is why we decided to give the same likelihood

343 to the three values of wind speed estimated in (6), instead of assuming a Gaussian or Weibull distribution of the probabilities
344 of wind speed in the grid cell. To fully capture this variability a complete coupling between the mesoscale and a detailed CFD
345 model would be needed - something that we may be able to do in the near future, but is still unavailable with current
346 computational resources. Another limitation of the present approach is that the CFD simulations used to build the database
347 from which the parametrization has been derived are all for a neutral atmosphere, so thermal effects on wind speed and its sub-
348 grid variability are neglected.

349 5. Conclusions

350 A new parameterization to quantify intra-neighbourhood heat stress variability in urban areas using a mesoscale model is
351 presented. This approach is based on two primary developments: 1) calculation of mean radiant temperature at several locations
352 within the idealized urban morphology used by the urban canopy model BEP-BEM; and 2) parameterization of mean wind
353 speed and its sub-grid spatial variability as a function of the local urban morphology and the mean wind velocity computed by
354 the WRF mesoscale model, using relations developed from a large suite of CFD simulations over a range of realistic and
355 idealized urban neighbourhoods. The components of the new parameterization have been validated against microscale model
356 results. From this approach the sub-grid variability of a heat stress index (i.e. UTCI or SET) can be computed for every grid
357 point, permitting quantification of the heat exposure at both cool and hot locations within each grid square at each time.

358 The new parameterization has been implemented in the multilayer scheme BEP-BEM in WRF and used to simulate a heatwave
359 day over Madrid (Spain) as proof of concept. The results of this initial application demonstrate the following:

- 360 I. The new parameterization gives information that is more suitable for the evaluation of heat stress than the air
361 temperature, being based on an index (UTCI or SET) that also combines air humidity, wind speed, and mean radiant
362 temperature.
- 363 II. The new parameterization provides substantively more information than air temperature alone (or any other index
364 that does not account for the mean radiant temperature). It provides information about the sub-grid variability (such
365 that heat stress in both cool and hot locations in each grid square is quantified). To our knowledge, this has not been
366 done before with a mesoscale model.
- 367 III. The results for the investigated case indicate a strong intraurban variability, both in air temperature and UTCI values,
368 that can be linked to the differences in urban morphology and elevation above sea level. The ability to assess the
369 differential impacts of urban morphology on heat stress is key to the provision of guidance for urban planning
370 strategies that mitigate urban overheating.
- 371 IV. Nadir-view surface temperature (i.e., as seen from a satellite-mounted remote sensor) is poorly correlated with both
372 air temperature and UTCI maps, indicating that, despite its ubiquitous use at present, it is unlikely to be an adequate
373 metric for heat impact assessment studies.

374 Finally, we consider that this new development introduces a new methodology for deploying mesoscale models to assess urban
375 overheating mitigation strategies.

376

377

378 ***Code Availability***

379 The code of WRF-comfort can be obtained here:

380 <https://doi.org/10.5281/zenodo.7951433>

381 The results of the simulation over Madrid shown in the manuscript are stored here:

382 <https://zenodo.org/record/8199017>

383

384 ***Competing interests***

385 The authors declare that they have no conflict of interest

386

388 **References**

- 389 Bougeault, P. and Lacarrere, P.: Parameterization of Orography-Induced Turbulence in a Mesobeta--Scale Model, *Mon.*
 390 *Weather Rev.*, 117, 1872–1890, [https://doi.org/10.1175/1520-0493\(1989\)117<1872:POOITI>2.0.CO;2](https://doi.org/10.1175/1520-0493(1989)117<1872:POOITI>2.0.CO;2), 1989.
- 391 Broadbent, A. M., Krayenhoff, E. S., and Georgescu, M.: The motley drivers of heat and cold exposure in 21st century US
 392 cities, *Proc. Natl. Acad. Sci. U. S. A.*, 117, 21108–21117, <https://doi.org/10.1073/pnas.2005492117>, 2020.
- 393 Brousse, O., Martilli, A., Foley, M., Mills, G., and Bechtel, B.: WUDAPT, an efficient land use producing data tool for
 394 mesoscale models? Integration of urban LCZ in WRF over Madrid, *Urban Climate*, 17, 116–134,
 395 <https://doi.org/10.1016/j.uclim.2016.04.001>, 2016.
- 396 Brown, M. J., Lawson, R. E., DeCroix, D. S., Lee, R. L., and Others: Comparison of centerline velocity measurements obtained
 397 around 2D and 3D building arrays in a wind tunnel, *Int. Soc. Environ. Hydraulics*, Tempe, AZ, 5, 495, 2001.
- 398 Coceal, O., Dobre, A., Thomas, T. G., and Belcher, S. E.: Structure of turbulent flow over regular arrays of cubical roughness,
 399 *J. Fluid Mech.*, 589, 375–409, <https://doi.org/10.1017/S002211200700794X> (doi:10.1017/S002211200700794X <<http://dx.doi.org/10.1017/S002211200700794X>>). , 2007.
- 400 J. Fluid Mech., 589, 375–409.
 401 (doi:10.1017/S002211200700794X <<http://dx.doi.org/10.1017/S002211200700794X>>). , 2007.
- 402 Franke, J., Hellsten, A., Schlünzen, H., and Carissimo, B.: The Best Practise Guideline for the CFD simulation of flows in the
 403 urban environment: an outcome of COST 732, in: *The Fifth International Symposium on Computational Wind Engineering*
 404 *(CWE2010)*, 1–10, 2010.
- 405 Frigo, M. and Johnson, S. G.: FFTW: an adaptive software architecture for the FFT, in: *Proceedings of the 1998 IEEE*
 406 *International Conference on Acoustics, Speech and Signal Processing, ICASSP '98 (Cat. No.98CH36181)*, 1381–1384 vol.3,
 407 <https://doi.org/10.1109/ICASSP.1998.681704>, 1998.
- 408 Gagge, A. P., Fobelets, A. P., Berglund, L., and Others: A standard predictive index of human response to the thermal
 409 environment, *ASHRAE Trans.*, 92, 709–731, 1986.
- 410 Geletič, J., Lehnert, M., Savić, S., and Milošević, D.: Modelled spatiotemporal variability of outdoor thermal comfort in local
 411 climate zones of the city of Brno, Czech Republic, *Sci. Total Environ.*, 624, 385–395,
 412 <https://doi.org/10.1016/j.scitotenv.2017.12.076>, 2018.
- 413 Giannaros, T. M., Lagouvardos, K., Kotroni, V., and Matzarakis, A. Operational forecasting of human-biometeorological
 414 conditions. *International journal of biometeorology*, 62, 1339-1343, 2018
- 415 Giannaros, C., Agathangelidis, I., Papavasileiou, G., Galanaki, E., Kotroni, V., Lagouvardos, K., ... and Matzarakis, A: The
 416 extreme heat wave of July–August 2021 in the Athens urban area (Greece): Atmospheric and human-biometeorological

417 analysis exploiting ultra-high resolution numerical modeling and the local climate zone framework. *Science of The Total*
418 *Environment*, 857, 159300, 2023.

419 Höpfe, P.: The physiological equivalent temperature - a universal index for the biometeorological assessment of the thermal
420 environment, *Int. J. Biometeorol.*, 43, 71–75, <https://doi.org/10.1007/s004840050118>, 1999.

421 Jendritzky, G., de Dear, R., and Havenith, G.: UTCI—Why another thermal index?, *Int. J. Biometeorol.*, 56, 421–428,
422 <https://doi.org/10.1007/s00484-011-0513-7>, 2012.

423 Jiang, T., Krayenhoff, E.S., Voogt, J.A., Warland, J., Demuzere, M. and Moede, C.: Dynamically downscaled projection of
424 urban outdoor thermal stress and indoor space cooling during future extreme heat. *Urban Climate*, 51, p.101648, 2023.

425 Jin, L., Schubert, S., Fenner, D., Salim, M. H., and Schneider, C.: Estimation of mean radiant temperature in cities using an
426 urban parameterization and building energy model within a mesoscale atmospheric model, *Meteorol. Z.*, 31, 31–52, 2022.

427 Kracht, O., Santiago, J., Martin, F., Piersanti, A., Cremona, G., Righini, G., Vitali, L., Delaney, K., Basu, B., Ghosh, B.,
428 Spangl, W., Brendle, C., Latikka, J., Kousa, A., Pärjälä, E., Meretoja, M., Malherbe, L., Letinois, L., Beauchamp, M., Lenartz,
429 F., Hutsemekers, V., Nguyen, L., Hoogerbrugge, R., Eneroth, K., Silvergren, S., Hooyberghs, H., Viaene, P., Maiheu, B.,
430 Janssen, S., Roet, D. and Gerboles, M., Spatial representativeness of air quality monitoring sites: Outcomes of the
431 FAIRMODE/AQUILA intercomparison exercise, EUR 28987 EN, Publications Office of the European Union, Luxembourg,
432 ISBN 978-92-79-77218-4, doi:10.2760/60611, JRC108791, 2017.

433 Krayenhoff, E. S., Moustou, M., Broadbent, A. M., Gupta, V., and Georgescu, M.: Diurnal interaction between urban
434 expansion, climate change and adaptation in US cities, *Nat. Clim. Chang.*, 8, 1097–1103, [https://doi.org/10.1038/s41558-018-](https://doi.org/10.1038/s41558-018-0320-9)
435 [0320-9](https://doi.org/10.1038/s41558-018-0320-9), 2018.

436 Krayenhoff, E. S., Jiang, T., Christen, A., Martilli, A., Oke, T. R., Bailey, B. N., ... and Crawford, B. R.: A multi-layer urban
437 canopy meteorological model with trees (BEP-Tree): Street tree impacts on pedestrian-level climate. *Urban Climate*, 32,
438 100590, 2023.

439 Kusaka, H., Kondo, H., Kikegawa, Y., & Kimura, F.: A simple single-layer urban canopy model for atmospheric models:
440 Comparison with multi-layer and slab models. *Boundary-layer meteorology*, 101, 329-358, 2001.

441 Lemonsu, A., Vigié, V., Daniel, M., and Masson, V.: Vulnerability to heat waves: Impact of urban expansion scenarios on
442 urban heat island and heat stress in Paris (France), *Urban Climate*, 14, 586–605, <https://doi.org/10.1016/j.uclim.2015.10.007>,
443 2015.

444 Leroyer, S., Bélaïr, S., Spacek, L., and Gultepe, I.: Modelling of radiation-based thermal stress indicators for urban numerical
445 weather prediction, *Urban Climate*, 25, 64–81, <https://doi.org/10.1016/j.uclim.2018.05.003>, 2018.

446 Lu, J., Nazarian, N., Hart, M.: OSM2LES - A Python-based tool to prepare realistic urban geometry for LES simulation from
447 OpenStreetMap (0.1.0). Zenodo. <https://doi.org/10.5281/zenodo.6566346>, 2022

448 Lu, J., Nazarian, N., Hart, M., Krayenhoff, S., Martilli, A.: Novel geometric parameters for assessing flow over realistic versus
449 idealized urban arrays. *Journal of Advances in Modeling Earth Systems*. <https://doi.org/10.1029/2022MS003287>, 2023.

450 Lu, J., Nazarian, N., Hart, M., Krayenhoff, S., Martilli, A.: Representing the effects of building height variability on urban
451 canopy flow. *Quarterly Journal of the Royal Meteorological Society*. <https://doi.org/10.1002/qj.4584>, 2023.

452 Maronga, B., Banzhaf, S., Burmeister, C., Esch, T., Forkel, R., Fröhlich, D., Fuka, V., Gehrke, K. F., Geletič, J., Giersch, S.,
453 Gronemeier, T., Groß, G., Heldens, W., Hellsten, A., Hoffmann, F., Inagaki, A., Kadasch, E., Kanani-Sühring, F., Ketelsen,
454 K., Khan, B. A., Knigge, C., Knoop, H., Krč, P., Kurppa, M., Maamari, H., Matzarakis, A., Mauder, M., Pallasch, M., Pavlik,
455 D., Pfafferoth, J., Resler, J., Rissmann, S., Russo, E., Salim, M., Schrempf, M., Schwenkel, J., Seckmeyer, G., Schubert, S.,
456 Sühring, M., von Tils, R., Vollmer, L., Ward, S., Witha, B., Wurps, H., Zeidler, J., and Raasch, S.: Overview of the PALM
457 model system 6.0, *Geosci. Model Dev.*, 13, 1335–1372, <https://doi.org/10.5194/gmd-13-1335-2020>, 2020.

458 Martilli, A., Clappier, A., and Rotach, M. W.: An Urban Surface Exchange Parameterisation for Mesoscale Models, *Bound.-*
459 *Layer Meteorol.*, 104, 261–304, <https://doi.org/10.1023/A:1016099921195>, 2002.

460 Martilli, A., Sánchez, B., Santiago, J. L., Rasilla, D., Pappaccogli, G., Allende, F., Martín, F., Roman-Cascón, C., Yagüe, C.,
461 and Fernández, F.: Simulating the pollutant dispersion during persistent Wintertime thermal Inversions over urban areas. The
462 case of Madrid, *Atmos. Res.*, 270, 106058, <https://doi.org/10.1016/j.atmosres.2022.106058>, 2022.

463 Masson, V.: A physically-based scheme for the urban energy budget in atmospheric models. *Boundary-layer meteorology*, 94,
464 357-397, 2000.

465 Matzarakis, A., Rutz, F., Mayer, H.: Modelling radiation fluxes in simple and complex environments—application of the
466 RayMan model. *Int. J. Biometeorol.* 51, 323–334. <https://doi.org/10.1007/s00484-006-0061-8>, 2007.

467 Middel, A. and Krayenhoff, E.S.: Micrometeorological determinants of pedestrian thermal exposure during record-breaking
468 heat in Tempe, Arizona: Introducing the MaRTy observational platform. *Science of the total environment*, 687, pp.137-151,
469 2019.

470 Nazarian, N., Fan, J., Sin, T., Norford, L., and Kleissl, J.: Predicting outdoor thermal comfort in urban environments: A 3D
471 numerical model for standard effective temperature, *Urban climate*, 2017.

472 Nazarian, N., Martilli, A., & Kleissl, J. (2018). Impacts of realistic urban heating, part I: spatial variability of mean flow,
473 turbulent exchange and pollutant dispersion. *Boundary-layer meteorology*, 166, 367-393.

474 Nazarian, N., Acero, J. A., and Norford, L.: Outdoor thermal comfort autonomy: Performance metrics for climate-conscious
475 urban design, *Build. Environ.*, 155, 145–160, <https://doi.org/10.1016/j.buildenv.2019.03.028>, 2019.

476 Nazarian, N., Krayenhoff, E. S., and Martilli, A.: A one-dimensional model of turbulent flow through “urban” canopies
477 (MLUCM v2.0): updates based on large-eddy simulation, *Geosci. Model Dev.*, 13, 937–953, [https://doi.org/10.5194/gmd-13-](https://doi.org/10.5194/gmd-13-937-2020)
478 937-2020, 2020.

479 Nazarian, N., Krayenhoff, E. S., Bechtel, B., Hondula, D. M., Paolini, R., Vanos, J., Cheung, T., Chow, W. T. L., de Dear, R.,
480 Jay, O., Lee, J. K. W., Martilli, A., Middel, A., Norford, L. K., Sadeghi, M., Schiavon, S., and Santamouris, M.: Integrated
481 assessment of urban overheating impacts on human life, *Earths Future*, 10, <https://doi.org/10.1029/2022ef002682>, 2022.

482 Piacsek, S. A. and Williams, G. P.: Conservation properties of convection difference schemes, *J. Comput. Phys.*, 6, 392–405,
483 [https://doi.org/10.1016/0021-9991\(70\)90038-0](https://doi.org/10.1016/0021-9991(70)90038-0), 1970.

484 Pigliautile, I., Pisello, A. L., and Bou-Zeid, E.: Humans in the city: Representing outdoor thermal comfort in urban canopy
485 models, *Renewable Sustainable Energy Rev.*, 133, 110103, <https://doi.org/10.1016/j.rser.2020.110103>, 2020.

486 Rodriguez-Sanchez, 2020, Simulación de olas de calor en la ciudad de Madrid, Master Thesis, Universidad Complutense de
487 Madrid,
488 https://www.researchgate.net/publication/353350538_Simulacion_de_olas_de_calor_en_la_ciudad_de_Madrid#fullTextFile
489 Content

490 Salamanca, F., Krpo, A., Martilli, A., and Clappier, A.: A new building energy model coupled with an urban canopy
491 parameterization for urban climate simulations—part I. formulation, verification, and sensitivity *Theor Appl Climatol* 99, 331–
492 344, <https://doi.org/10.1007/s00704-009-0142-9>, 2010.

493 Salamanca, F., Martilli, A., and Yagüe, C.: A numerical study of the Urban Heat Island over Madrid during the DESIREX
494 (2008) campaign with WRF and an evaluation of simple mitigation strategies, *International Journal of Climatology*, 32, 2372–
495 2386, <https://doi.org/10.1002/joc.33982>, 2012.

496 Santiago, J.L., Rivas, E., Sanchez, B., Buccolieri, R. and Martin, F.: The impact of planting trees on NOx concentrations: The
497 case of the Plaza de la Cruz neighbourhood in Pamplona (Spain). *Atmosphere*, 8(7), p.131.
498 <https://doi.org/10.3390/atmos8070131>, 2017.

499 Santiago, J.L., Sanchez, B., Quaassdorff, C., de la Paz, D., Martilli, A., Martín, F., Borge, R., Rivas, E., Gómez-Moreno, F.J.,
500 Díaz, E. and Artiñano, B., Yagüe, C. and Vardoulakis, S.: Performance evaluation of a multiscale modelling system applied
501 to particulate matter dispersion in a real traffic hot spot in Madrid (Spain). *Atmos. Pollut. Res.*, 11 (1), pp. 141-155.
502 <https://doi.org/10.1016/j.apr.2019.10.001>, 2020.

503 Sanchez, B., Santiago, J.L., Martilli, A., Martin, F., Borge, R., Quaassdorff, C. and de la Paz, D, 2017. Modelling NOx
504 concentrations through CFD-RANS in an urban hot-spot using high resolution traffic emissions and meteorology from a
505 mesoscale model. *Atmos. Environ.*, 163, pp. 155-165. <https://doi.org/10.1016/j.atmosenv.2017.05>, 2022

506 Sanchez, B., Santiago, J.L., Martilli, A., Palacios, M., Núñez, L., Pujadas, M. and Fernández-Pampillón, J.: NO_x depolluting
507 performance of photocatalytic materials in an urban area - Part II: assessment through computational fluid dynamics
508 simulations. *Atmos. Environ.*, 246 (2021), p. 118091. <https://doi.org/10.1016/j.atmosenv.2020.118091>, 2021.

509 Santiago, J. L., Krayenhoff, E. S., & Martilli, A. (2014). Flow simulations for simplified urban configurations with microscale
510 distributions of surface thermal forcing. *Urban Climate*, 9, 115-133. <https://doi.org/10.1016/j.uclim.2014.07.008>

511 Skamarock, W. C., Klemp, J. B., Dudhia, J., Gill, D. O., Liu, Z., Berner, J., Wang, W., Powers, J. G., Duda, M. G., Barker, D.
512 M., and Others: A description of the advanced research WRF model version 4, National Center for Atmospheric Research:
513 Boulder, CO, USA, 145, 550, 2019.

514 Thorsson, S., Lindberg, F., Eliasson, I., & Holmer, B.: Different methods for estimating the mean radiant temperature in an
515 outdoor urban setting. *International Journal of Climatology: A Journal of the Royal Meteorological Society*, 27(14), 1983-
516 1993, 2007.

517 Tuholske, C., Caylor, K., Funk, C., Verdin, A., Sweeney, S., Grace, K., Peterson, P., and Evans, T.: Global urban population
518 exposure to extreme heat, *Proc. Natl. Acad. Sci. U. S. A.*, 118, <https://doi.org/10.1073/pnas.2024792118>, 2021.

519 Zhang, J., Li, Z., and Hu, D.: Effects of urban morphology on thermal comfort at the micro-scale, *Sustainable Cities and*
520 *Society*, 86, 104150, <https://doi.org/10.1016/j.scs.2022.104150>, 2022.

521 Zhao, L., Oleson, K., Bou-Zeid, E., Krayenhoff, E. S., Bray, A., Zhu, Q., Zheng, Z., Chen, C., and Oppenheimer, M.: Global
522 multi-model projections of local urban climates, *Nat. Clim. Chang.*, <https://doi.org/10.1038/s41558-020-00958-8>, 2021.

523

524

525

526 Appendix A. *Computation of Radiation for Mean Radiant Temperature*

527 As explained in the text, the mean radiant temperature at pedestrian level is represented using formula (1). The full expression
528 of the longwave radiation components for the vertical faces of the pedestrian (L_1, L_2), for the case of an urban morphology
529 with buildings of constant height and walls with no windows, is as follows:

530
$$L_1 = \sum_{i=1,n} \psi_{1i,p} \varepsilon_W (Rl_{1W_i} + \sigma T_{1i}^4) + \psi_{1G,p} \varepsilon_G (Rl_G + \sigma T_G^4) + \psi_{1S,p} Rl_S$$

531
$$L_2 = \sum_{i=1,n} \psi_{2i,p} \varepsilon_W (Rl_{2W_i} + \sigma T_{2i}^4) + \psi_{2G,p} \varepsilon_G (Rl_G + \sigma T_G^4) + \psi_{2S,p} Rl_S$$

532 Where (see Fig A1).:

533 $\psi_{1i,p}$ = is the view factor from wall section i of building 1 to the side 1 of the pedestrian

534 ε_W = is the emissivity of the wall

535 Rl_{1W_i} = is the long wave radiation reaching the section i of the wall of building 1

536 T_{1i} = is the surface temperature of the section i of the wall of building 1

537 $\psi_{1G,p}$ = is the view factor from the ground (or street) to the side 1 of the pedestrian

538 ε_G = is the emissivity of the ground

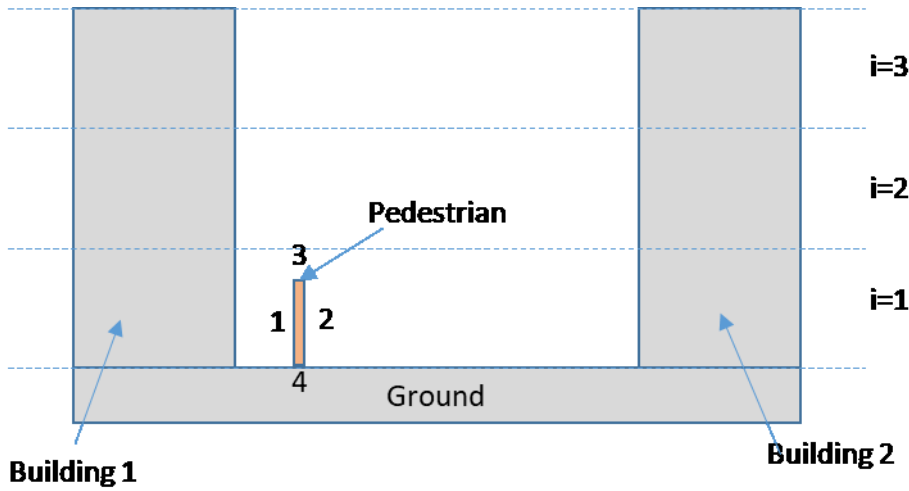
539 Rl_G = is the longwave radiation reaching the ground (street)

540 T_G = is the surface temperature of the ground (street)

541 $\psi_{1S,p}$ = is the view factor from the sky to side 1 of the pedestrian

542 Rl_S = longwave radiation from the sky

543 σ = is the Stefan-Boltzmann constant.



544

545 *Figure A1. Schematic of the Street canyon.*

546 Similar meaning applies for side and building 2.

547 The values of the surface temperatures and the longwave radiations are computed with BEP_BEM. The view factors are
 548 estimated based on formulas A13-A19 of Martilli et al. 2002, using a height for the pedestrian of 1.8 m.

549 For the longwave radiation reaching the top of the pedestrian, we made the simple assumption that it is equal to the radiation
 550 coming from the sky, $L_3 = Rl_s$, while for the longwave radiation reaching the bottom of the pedestrian, the assumption is that
 551 it is equal to the radiation emitted and reflected by the ground, or $L_4 = \varepsilon_G Rl_G + \varepsilon_G \sigma T_G^4$. We consider that these assumptions
 552 are reasonable, giving that the contribution of the radiation reaching the top and bottom of the pedestrian is only 6% each to
 553 the final value of the mean radiant temperature.

554 A similar approach is followed for the short wave radiation, leading to:

555

556
$$K_1 = \sum_{i=1,n} \psi_{1i,p} \alpha_i R_{S_{1W_i}} + \psi_{1G,p} \alpha_G R_{S_G} + R_{S_{1S}}$$

557
$$K_2 = \sum_{i=1,n} \psi_{2i,p} \alpha_i R_{S_{2W_i}} + \psi_{2G,p} \alpha_G R_{S_G} + R_{S_{2S}}$$

558 Where

559 $R_{S_{1W_i}}$ =short wave radiation reaching the section i of the wall of building 1

560 α_i =albedo of the section i of the wall of the building

561 R_{S_G} = is the short wave radiation reaching the ground

562 α_G = is the albedo of the ground

563 Rs_{1S} = is the short wave radiation from the sun reaching directly side 1 of the pedestrian, computed using formula A10 of
564 Martilli et al. 2002, using a height of the pedestrian of 1.8m.

565 Similar meaning for side and wall 2.

566 Regarding the radiation reaching the top of the pedestrian, K_3 , for simplicity only the radiation coming directly from the sun
567 is considered, without accounting for the reflection from the walls. So the value is zero if the pedestrian is in full shadow, and
568 to estimate it, the formula used is from A11 of Martilli et al. 2002. The value of the radiation reaching the bottom of the
569 pedestrian is the value reflected by the ground, or $K_3 = \alpha_G Rs_G$,

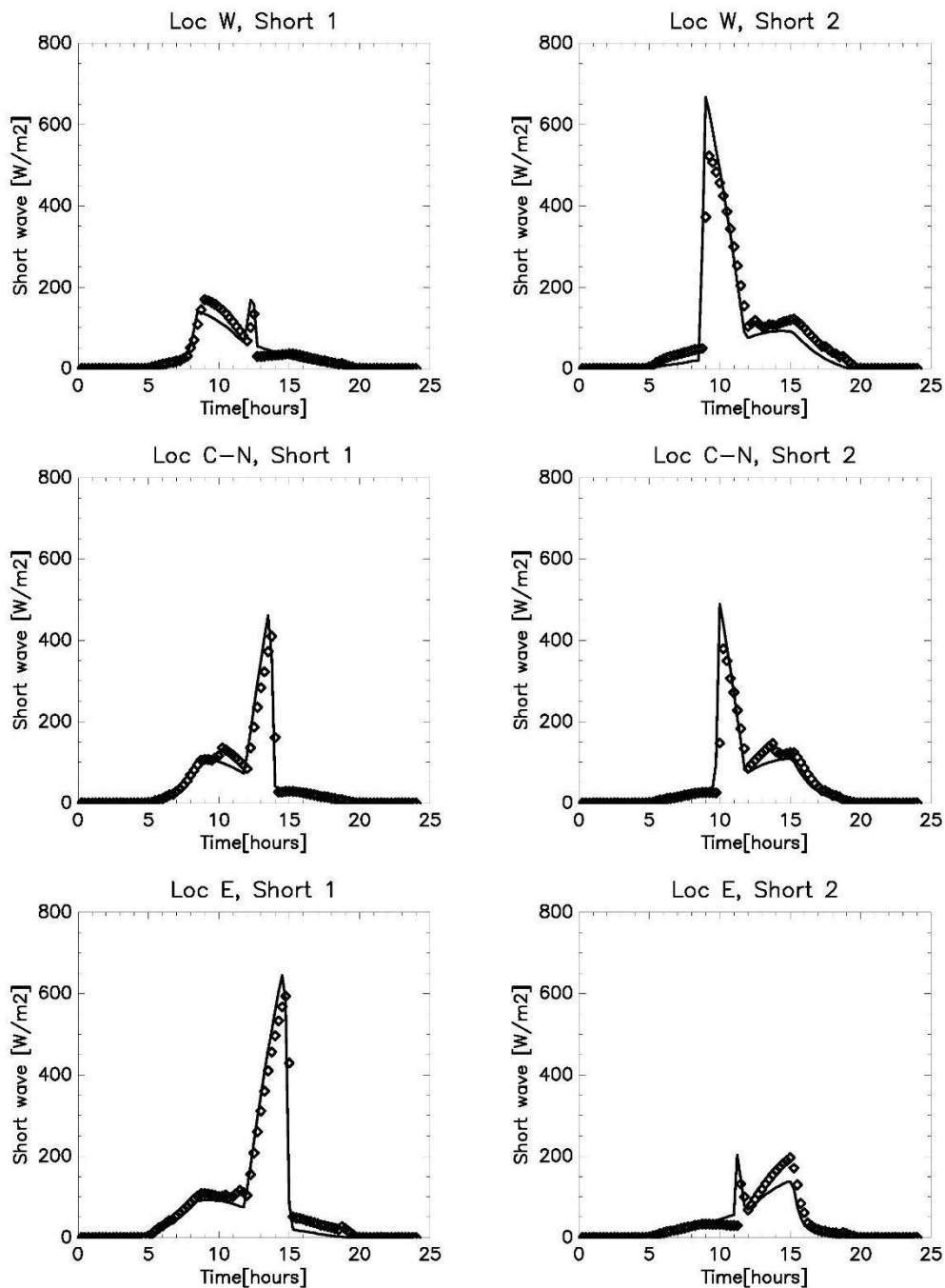
570

571

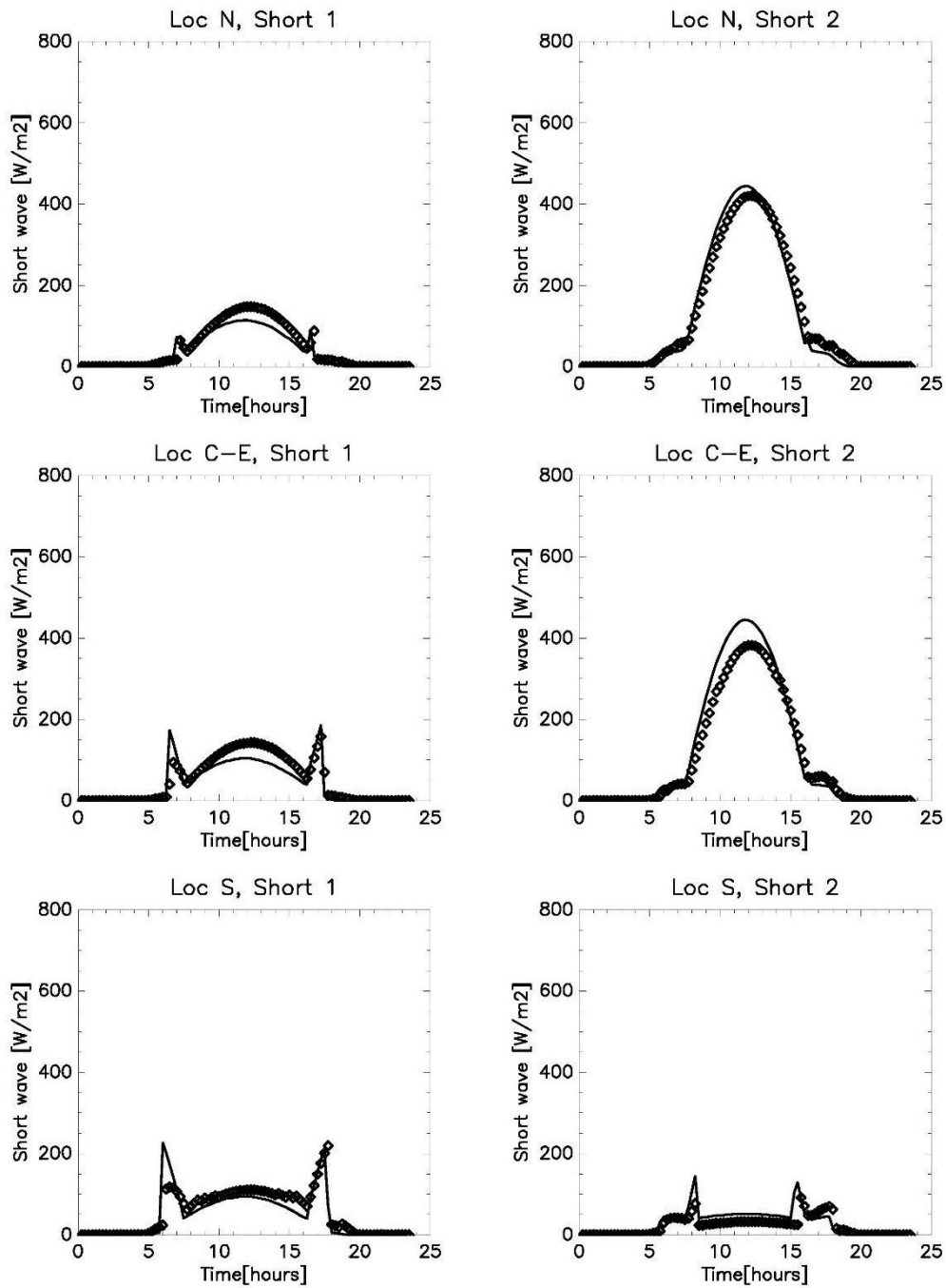
572

573 *Appendix B. Comparison of Short wave calculation in BEP-BEM and TUF-pedestrian.*

574 Short wave radiation is an essential component of the MRT. Below we compare the short wave radiation reaching the vertical
575 sides of the segment representing the human body computed by BEP-BEM vs those estimated with the more detailed model
576 TUF-pedestrian.



577
 578 Figure B1. Comparison of short wave radiation at the two sides of the vertical segment representing the pedestrian for the N-
 579 S oriented street. Solid line is the WRF, while diamonds are TUF. Short 1 means the side 1 of the pedestrian, while Short 2
 580 the side 2.



581

582







583 Figure B2. Same as B1, but for an E-W oriented street

584

Appendix C. *CFD simulations for wind speed variability*

Data from over 173 microscales CFD simulations of urban airflow are considered over realistic and idealized urban configurations, spanning a wide range of building plan area (λ_p), frontal area (λ_f), and wall area (λ_w) densities representative of realistic urban neighborhoods in different types of cities. CFD simulations are conducted using 162 large-eddy simulations (LES) and 11 Reynolds-averaged Navier–Stokes (RANS) schemes detailed in Table B.1.

Table B.1 Details of CFD microscale simulation cases considered in this study. Simulations are classified based on the configuration (urban form) used. These classifications include **UA** (Uniform height with **A**ligned configuration), **US** (Uniform height with **S**taggered configuration), **VA** (Variable height with **A**ligned configuration), **VS** (Variable height with **S**taggered configuration), **UR** (Uniform height with **R**ealistic configuration), and **VR-WD** (Variable height with **R**ealistic configuration and multiple **W**ind **D**irections considered).

Model	Classification	H_m [m]	H_{max} [m]	λ_p range	Count	Source	Example
LES	UA	16	16	[0.0625 - 0.64]	7	Nazarian et al. 2020 Lu et al. 2022	
LES	US	16	16	[0.0625 - 0.64]	7	Nazarian et al. 2020 Lu et al. 2022	
LES	VA	16	20, 24	[0.0625 - 0.64]	42	Lu et al. 2022 Lu et al. 2023	
LES	VS	16	20, 24	[0.0625 - 0.64]	42	Lu et al. 2022 Lu et al. 2023	
LES	UR	16	16	[0.057 - 0.536]	64	Lu et al. 2022	
RANS	VR-WD	14.5-34	variable	[0.190 - 0.680]	11	Sanchez et al. (2017) Santiago et al. (2017) Kracht et al. (2017) Borge et al. (2018) Kracht et al. (2019) Santiago et al. (2020) Sanchez et al. (2021)	

591

In the LES simulations, airflow over idealized and realistic urban arrays to determine the model parameters (Nazarian et al., 2020; Lu et al., 2022, 2023). Realistic urban layouts are prepared by rasterizing building footprints from an open-source dataset OpenStreetMap using OSM2LES (Lu et al., 2022). 64 realistic urban neighbourhoods were obtained assuming uniform building height (Table B.1) from several major cities such as Sydney and Melbourne (Australia), Barcelona (Spain), Detroit,

596 Los Angeles, and Chicago (United States). Idealized urban arrays are considered in aligned and staggered arrangement that
597 follows (Coceal et al., 2007) with varying urban density (λ_p in [0.0625,0.64]) and height variability ($H_{std}=[0m,2.8m,5.6m]$).
598 Simulations are conducted in the Parallelized Large-eddy Simulation Model (PALM, version r4554) (Maronga et al., 2020)
599 following the same setup in (Nazarian et al., 2020), which has validated results against Direct Numerical Simulation (Coceal
600 et al., 2007) and wind tunnel experiments (Brown et al., 2001). The computational domain is discretized using the second-
601 order central differences (Piacsek and Williams, 1970) where the horizontal grid spacing is uniform and the vertical spacing
602 follows the staggered Arakawa C-grid. The minimal storage scheme is employed in the time integration to solve the filtered
603 prognostic incompressible Boussinesq equations where the pressure perturbation was calculated in Poisson's equation and was
604 solved by the FFTW scheme (Frigo and Johnson, 1998).

605 The RANS dataset is derived from steady-state CFD-RANS simulations performed with the Realizable k- ϵ turbulence model
606 (STAR-CCM+, Siemens) over realistic urban areas. The size of the computational domains is determined following the best
607 practice guideline of COST Action 732 (Franke et al., 2010). The horizontal area covers around 1-1.5 km² and the domain top
608 is at around 8H, being H the mean height of buildings. The resolution of the irregular polyhedral mesh used in all CFD-RANS
609 simulations goes from 0.5 m close to buildings to 6 m out of the built-up area, which results in between 3 and 8 million grid
610 points depending on the complexity of the geometry. Inlet vertical profiles for wind speed, turbulent kinetic energy (k), and
611 its dissipation (ϵ), are established in neutral atmospheric conditions. The evaluation of the CFD-RANS simulations was
612 addressed in previous studies summarized in Table B2 and more information is provided in previous publications.

613